Microstructure, Properties, and Mechanisms of TiC-Mo-Ni Cermets Produced by SHS

J. C. LaSalvia and M. A. Meyers

Institute for Mechanics and Materials
Department of Applied Mechanics and Engineering Sciences
University of California, San Diego

Dense TiC-Ni-based cermet articles were produced by self-propagating high-temperature synthesis (SHS) combined with impact forging. The focus of this investigation was two-fold: (1) densify porous SHS TiC-Ni-based articles by impact forging; and (2) improve microstructure and mechanical properties by Mo additions. Mo additions were varied between 0-10 wt.% in 2 wt.% increments, while the Ni content was fixed at 30 wt.%. Cylindrical tiles 6.35 cm diameter, 1.2 cm thickness (~220 g) with apparent densities >99% were easily produced. Microstructures consisted of a spheroidal carbide phase embedded in a Ni alloy binder. Mo did not have a strong effect on carbide particle size (3.5-4.5 μm) or morphology. Compressive strength, transverse-rupture strength, fracture toughness, and Young's modulus improved with increasing Mo content. Aspects of the densification process, evolution of the mesolevel structures within the different regions of the combustion wave, and characterization of the final products are discussed.

1. INTRODUCTION

Self-propagating high-temperature synthesis (SHS), is the process by which condensed phases are

produced by self-sustaining exothermic chemical reactions. The main unique characteristic of SHS is that the reactions are self-propagating: once the reaction is initiated within one part of a reactive mixture, it readily propagates into the surrounding mixture in the form of a combustion wave. By this process, many industrially important materials such as borides, carbides, cermets, intermetallics, nitrides, silicides, and composites have been produced [1-5].

Many researchers in SHS have focused on the elucidation of the physical processes which occur during the propagation of the combustion wave [6-8]. The motivation has been to understand at a fundamental level the effect of various parameters on the main reaction mechanisms and product evolution. This is in line with the overall goal of producing quality materials and products by SHS through better control the process.

One of the main disadvantages of using SHS to produce structural engineering parts in a single step process is that the resulting parts are typically porous (with the exception of SHS casting or reactive sintering). Figure 1 is an optical micrograph obtained from a TiC-30Ni-14Mo (weight percent) material produced by SHS (dark areas are residual porosity). This residual porosity is due to several factors: (a) initial green body porosity; (b) lower specific volume of the product phase; and (c) outgassing of volatilized impurities.

A number of methods have been developed in Russia, Japan, China, and the United States to densify and form the porous materials during or after the SHS process, while the material still exists in a ductile state [9-26]. In the United States, pressureless and pressure-assisted reactive sintering, conventional and quasi-isostatic hot-pressing, impact or high-rate forging, and explosive compaction have been successfully used to obtain dense materials [16-26]. Figure 2(a) is a back-scattered electron micrograph of a TiC-30Ni cermet obtained by impact forging [23]. The microstructure consists of a spheroidal TiC phase embedded in a Ni-alloy binding phase. The apparent density is greater than 99%.

The high degree of contiguity of the TiC phase in Fig. 2(a) indicates a less than optimum distribution of the Ni-alloy phase which leads to a degradation in the mechanical performance. In the 1950s, Humenik and Parikh [27,28] showed that by replacing 10 wt.% of the melt with Mo, complete wetting (i.e., contact angle to 0°) was obtained. As a result, both TiC particle coarsening and contiguity were substantially decreased. This improvement in the microstructure resulted in an enhancement in mechanical performance which subsequently led to industrial use [29-33].

The purpose of this investigation is two-fold: (i) to determine the effect of Mo additions on the microstructures and mechanical properties of TiC-Ni-based cermets produced by the SHS/impact forging technique; and (ii) to determine the physical processes which not only occur within the combustion wave but which also influence the formation of the final microstructure.

2. EXPERIMENTAL PROCEDURES

High-purity (99.7%) Ti (Micron Metals Inc., Salt Lake City, Utah), (99.9%) C in graphite form (Consolidated Astronautics, Smithtown, NY), (99.5%) Ni (Aldrich Chemical Co., Milwaukee, WI), and (99.9%) Mo (Cerac/Pure Division, Milwaukee, WI) powders were used in this investigation. The Ti, C, Ni, and Mo powder sizes were $< 44 \ \mu$m (-325 mesh), 2 μm, 3 μm, and 2-4 μm, respectively.

The powders (400 g batches) were dry mixed in a polyethylene bottle under an Ar atmosphere for 24 hours using a grinding medium (2:1 mass ratio). After mixing, the powder was placed into a vacuum oven (100 mm Hg, 100°C) for 24 hours to remove any absorbed water. Green cylindrical tiles 6.35 cm in diameter and approximately 2.3 cm thick ($\sim$220 g) with densities of 65% of the theoretical were produced by uniaxially compacting in a steel die using a pressure of 55 MPa.
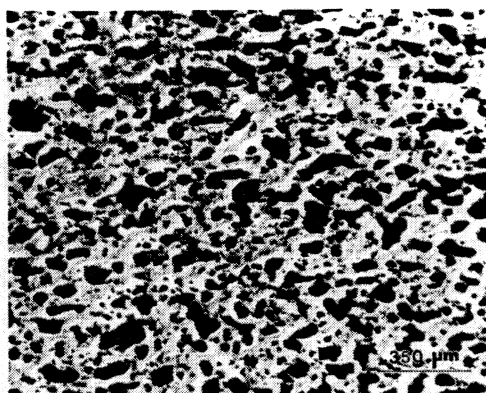
Fig. 1. Optical micrograph obtained from a TiC-30Ni-14Mo combustion synthesized compact.

Details of the SHS/impact forging technique are given elsewhere [20-22]. In this technique, the time delay between the initiation of the SHS process and when densification is initiated is critical for obtaining a fully reacted, fully dense bodies. Issues concerning reaction completion, composition evolution, and material ductility determine the extent of this time delay. Preliminary experiments showed that a time delay between 8-15 seconds yields fully reacted dense compacts (longer time delays resulted in fully dense cracked tiles). In this investigation, a time delay of 15 seconds was used.

Densified disks were sectioned for metallographic, scanning electron microscopy, X-ray diffraction, and apparent density measurements. For a reliable comparison basis, specimens were taken from the central region of each disk. Particle size measurements were performed using the linear-intercept technique.

Vickers microhardness measurements (500 gf load) were conducted to examine the effect of Mo on hardness. Quasi-static compression and four-point bend tests were limited to the 0 Mo, 4 Mo, and 8 Mo materials. The top and bottom surfaces of the densified compacts were ground flat and parallel to within 5 μm. Compression (4 mm $\times$ 4 mm $\times$ 7 mm) and four-point bend (4 mm $\times$ 7 mm $\times$ 30 mm) specimens were cut from the ground compacts by electro-discharge machining. Both compression and four-point bend tests (a minimum of 3 experiments per test per material) were conducted using a screw-driven Instron compression/tension mechanical testing machine. The loading ends of the compression specimens were polished using 1 μm and 0.25 μm diamond pastes. This was done to eliminate the surface flaws introduced during flat grinding. Load bearing platens (i.e., micrograined WC-10Co) were used in the compression tests. These platens were ground flat and parallel to 15 μm. Stainless steel shims 25 μm thick were used between the specimen and the platens. Tests were conducted at a loading rate of 4 μm/sec which corresponded to a strain-rate of approximately 5×10^{-3} s^{-1}. Alignment of the specimen and platens with the loading axis of the machine was performed by sight. The four-point bend fixture used high carbon steel rods 3 mm in diameter as bottom simple supports and loading points. The bottom supports and loading points were 25.4 mm and 12.7 mm apart, respectively. Tests were conducted at a loading rate of 4 μm/sec. The elastic moduli were determined using an ultrasonic technique in which both the longitudinal and shear wave speeds were measured [34].

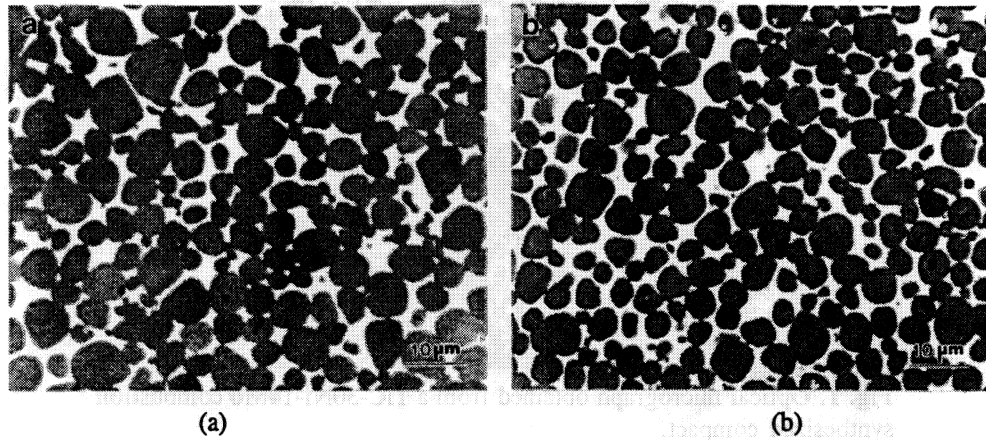(a)   (b)

Fig. 2. Back-scattered electron micrographs for the combustion
synthesized/impacted forged (a) 0 Mo and (b) 8 Mo.

The reaction arresting technique used in this investigation was extremely simple and is based on
the approach developed by Rogachev et al. [6,7]. Their approach consists of placing the reactant
powder mixtures into a Cu cylinder with a conical hole. After ignition (at the base of the cone), the
combustion wave propagates down the cone axis, in the direction of decreasing diameter. As a result,
the rate of heat loss increases since the cone contact surface area per unit volume of reactant mixture
increases. When the characteristic times for the reaction and cooling become of the same order, the
reaction will not go to completion. These experiments were conducted under an Ar atmosphere to
prevent oxidation of the specimen. After each experiment, the specimen was infiltrated with epoxy,
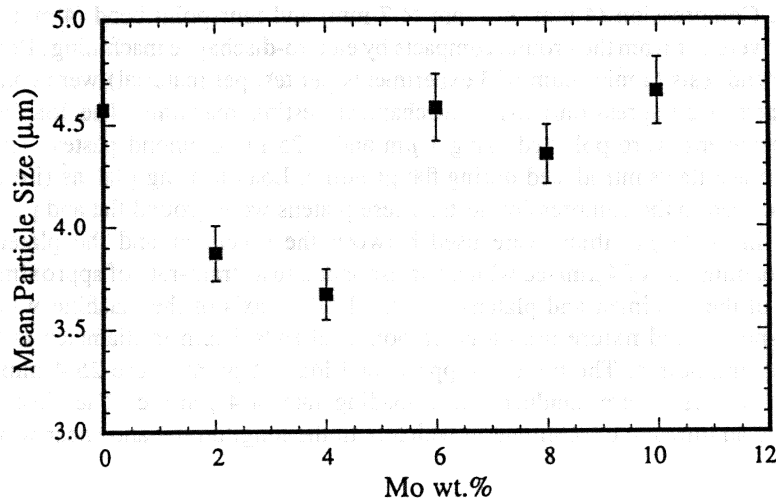

Fig. 3. Effect of the Mo on carbide particle size of the combustion
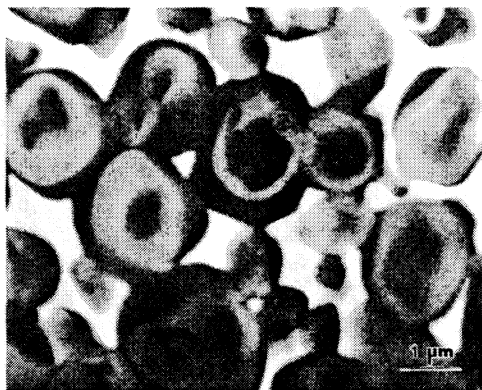synthesized/impacted forged TiC-Ni based materials.

Fig. 4. Mo-rich region found in the combustion synthesized/impacted forged materials.

sectioned longitudinally, and polished using standard metallographic techniques. Specimens were carbon coated for observation by scanning electron microscopy (SEM).

3. RESULTS AND DISCUSSION

3.1. Microstructure

Qualitatively, the resulting SHS/impact forged microstructures do not appear to be very different; they consist of a spheroidal carbide phase embedded in a highly continuous Ni-alloy binding phase. Back-scattered electron micrographs for the 0 and 8 Mo materials are shown in Fig. 2(a) and (b), respectively. The dramatic influence of Mo on the TiC particle size observed by Humenik and Parikh [27] is not obtained. This is due to the fact that the processing techniques are entirely different as will be shown later.

Figure 3 shows the results of the particle size measurements. The error bars denote a 95% confidence level that the mean lies within ±4% of its specified value. The mean particle size for these materials ranges between 3.5 and 4.5 μm. Conventionally produced TiC-based cermets typically possess particle sizes between 1 and 2 μm. Liquid-phase sintering temperatures for TiC-based cermets are typically around 1350°C in order to minimize carbide particle coarsening [29-33]. The maximum temperature within the combustion wave greatly exceeds this value ($T_{ad} \approx 2500$°C [35]); thus, a larger particle size would be expected assuming that the physical processes which govern the evolution of the microstructure during the SHS process are the same as in conventional processing.

Evidence for the incomplete solutionizing of Mo within the Ni-alloy melt is observed. One such region found in the 2 Mo material is shown in Fig. 4. The mean size of these particles is approximately 1 μm. These particles exhibit a multiple core-shell structure. Some of the particles appear to have a structure which is the reverse of that expected (i.e., Mo-rich core and Mo-poor shell). These regions are due to Mo agglomerates which were not broken up and uniformly dispersed during the mixing process. The temperature-time history is not sufficient to completely dissolve the largest Mo agglomerates (Mo melting temperature ≈ 2600°C).

(a)

(b)

(c)
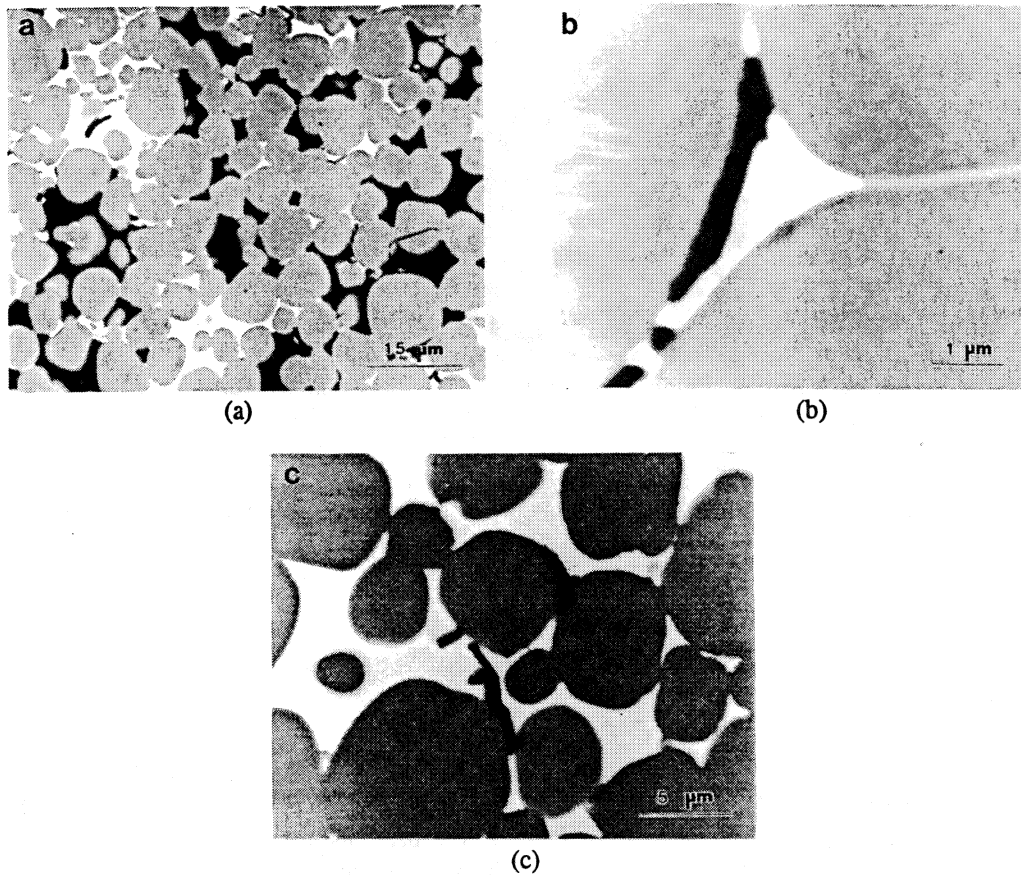
Fig. 5. Microstructural flaws observed within the 0 Mo material: (a) region devoid of Ni-alloy binder; (b) Interphase debonding; and (c) partial interphase debonding and microcracks within the Ni-alloy binder.

A decrease in the number of microstructural flaws such as voids, interphase debonding, and binder microcracks is observed with increasing Mo content. This is attributed to the improvement in wetting of the Ni-alloy binder on the carbide phase. Figure 5 shows typical flaws observed primarily within the 0 Mo material. Figure 5(a)-(c) show an area devoid of the Ni-alloy binder, partial debonding between the Ni-alloy binder and a TiC particle, and partial debonding between phases, as well as a microcrack penetrating into the Ni-alloy binder, respectively. Both the interphase debonding and the microcracks within the Ni-alloy binder are evidence that large residual tensile stresses existed within it as a result of the difference in the thermal expansion behavior between the two phases [36].

3.2. Mechanical Properties and Fracture Morphology Characterization

The measured mechanical properties for the 0 Mo, 4 Mo, and 8 Mo materials are listed in Table 1. The improvement in mechanical properties with increasing Mo content is believed to be due to the

Table 1. Summary of mechanical properties for the 0, 4, and 8 Mo materials.

Mo content (wt%)	D (μm)	ρ (kg/m³)	HV500 (GPa)	σ_c (MPa)	σ_B (MPa)	K_c (MPa·m$^{1/2}$)	E (GPa)	G (GPa)	ν
0	4.6±0.15	5550	13.1±1.6	2940±110	470±95	9±1	311	120	0.3
4	3.7±0.1	5730	13±1.1	3250±110	815±30	11±2	321	123	0.3
8	4.35±0.15	6050	13.3±1.4	3380±90	1330±70	22±1	340	131	0.3

increase in interphase bond strength and to the decrease in the number of microstructural flaws (supported by the microstructural observations above). A substantial increase in the transverse rupture strength between the 0 Mo and 8 Mo materials is obtained. The transverse rupture strength is extremely sensitive to preexisting flaws. Fracture toughness estimates were made possible from the transverse rupture strength measurements due to the observation of failure initiating flaws on the fracture surfaces. Overall, the mechanical properties for the 8 Mo material are comparable to conventionally produced cermets with similar compositions [29-33,37-40].

For the compositions investigated, the addition of Mo does not significantly affect the hardness. The mean Vickers microhardness of the specimens is approximately 13 GPa, which is equivalent to a Rockwell Hardness "A" scale number ≈ 87-88 [37].

Figure 6 is of a crack within a 0 Mo compression specimen which did not propagate sufficiently to cause failure (loading axis is approximately top to bottom). Crack branching is clearly seen. Carbide particle fracture (arrows 1), interphase debonding (arrows 2), and microcracks within the Ni-alloy binder (arrows 3) can be seen.

3.3. Micromechanisms of SHS in the Ti-C-Ni-Mo System

A computational heat transfer analysis was conducted on the reaction arresting configuration, to estimate the characteristic cooling times. The specimen and Cu block were modelled as an inner solid cylinder and outer concentric cylinder, respectively. The effect of the taper on the cooling rate was determined by considering only radial heat conduction while varying the diameter of the specimen. The initial temperatures of the inner and outer cylinders were set at 2000°C and 25°C, respectively. The simulation predicts that the temperature decreases from the maximum to room temperature in approximately 1-2 seconds depending on location along the cone axis. The maximum cooling rates vary from approximately 3×10^3 K/s near the base of the cone, to 10^4 K/s near its apex. These cooling rates are of the same order as those obtained in the experimental studies of Mukasyan and Borovinskaya [41] and Merzhanov *et al.* [42]. The variation in cooling rates along the cone axis allows the "bracketing" of the reaction at different stages of its progression.

In general, the macrostructure of the specimens consisted of a fully reacted region, a partially reacted region, and an unreacted region (regions 1, 2, and 3, respectively, in Fig. 7). No distinct interface exists between the fully reacted and partially reacted regions. This is due to the distribution in C agglomerate sizes. A distinct interface does exist between the partially reacted region and the unreacted region due to the formation of a Ni-Ti melt. Negligible interaction between components is observed within the unreacted region, being limited only to contact regions. In the following discussion, the reported observations will start with the unreacted region and proceed towards the fully reacted region.
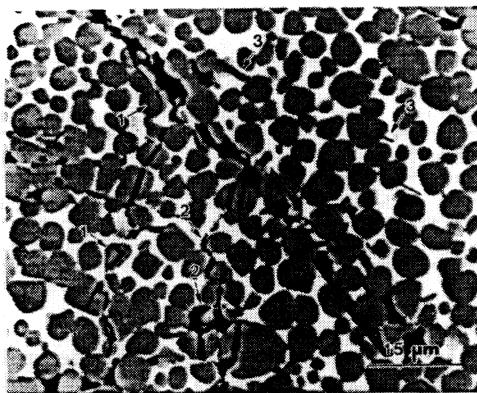
Fig. 6. Macrocracks with crack branching within a 0 Mo compression specimen. Carbide particle fracture (arrows 1), interphase debonding (arrows 2), and microcracks within the Ni-alloy binder (arrows 3) can be seen.

3.3.1. Unreacted Region

The first process observed to occur within the unreacted region is a reaction at the surface of the Ti particles. The uniformity of the reaction around the particles indicates that the reaction must be proceeding via the gas phase. Impurity analysis by the powder manufacturer indicates that H_2 (0.04 wt.%) impurity is mainly contained at the surface of the particles [43]. In studies of the volatile impurity emissions during the SHS of TiC by Kecskes and Niiler [44] and of TiB_2 by Filonenko and
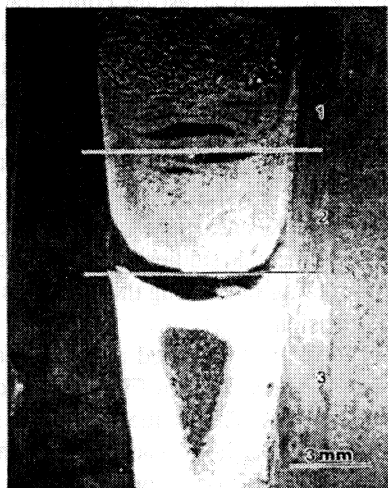
Fig. 7. Macroscopic view of cross-section of the Ti-C-Ni-Mo specimen after reaction.
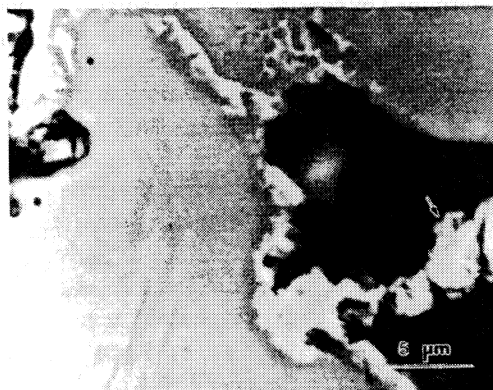
Fig. 8. Interaction between Ni and Ti at the contact region (initial Ti-Ni melt formation).
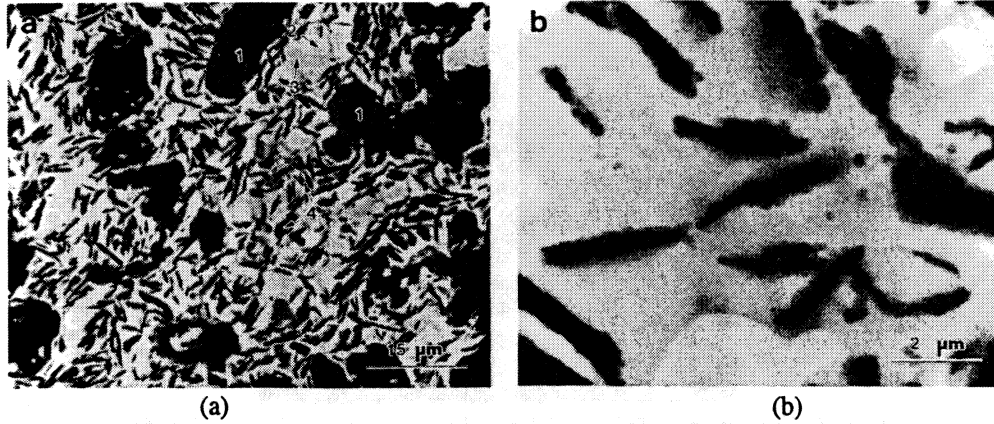
(a)   (b)

Fig. 9. (a) Partially reacted region showing the porosity (1), Ti-Ni melt formation (2) and (3), and C (graphite) flakes (4); and (b) TiC_x layer converging the C particles.

Vershinnikov [45], H_2 was one of the major gaseous impurities emitted during the reactions which occurs at a low temperature.

Evidence for the α(HCP) $\rightarrow \beta$(BCC) (transformation occurs at approximately 893 °C) solid phase transformation of Ti is observed next. The structure is either α platelets separated by the β phase (Widmanstatten structure) or α' platelets separated by the β phase. This structure indicates that the Ti particle was subjected to a thermal cycle in which it was heated to a sufficiently high temperature such that it underwent the $\alpha \rightarrow \beta$ transformation and then was rapidly cooled. The sharpness of the particles indicates that the surface scale has been completely removed before entering into the partially reacted region.

3.3.2. Partially Reacted Region

The onset of the partially reacted region is generally characterized by the interaction of Ni with the Ti particles. As would be expected, the initial reaction between the Ni and Ti particles occurs at regions of contact and results in the formation of Ti-Ni compounds. A localized Ni-Ti melt forms which subsequently spreads over the surface of the Ti particles. Figure 8 is a close-up of the Ni-Ti reaction. The Ni particle in Fig. 8 (shown by arrow) indicates that the local temperature is below the melting point for Ni. According to Merzhanov *et al.* [42], melt spreading and product formation are inseparable processes. The spreading force F_s is given by the difference between the energies of adhesion W_A and of cohesion W_C (neglecting potential and kinetic energies). The energy of adhesion is the sum of the energies of intermolecular interaction (e.g., adsorption) W_A^M and chemical bond formation W_A^B. The energy of cohesion is taken to be twice the liquid-gas interfacial energy γ_{lg}. Therefore, $F_s = W_A^M + W_A^B - 2\gamma_{lg}$. Note that for good wetting systems, γ_{lg} is smaller than for poor wetting systems [46]. The condition for spreading is that the spreading force F_s be greater than zero. Typically, for liquid metals, $W_C \approx 10^3$ mJ/m^2 while $W_A^M \approx 10^2$ mJ/m^2 [42]. Consequently, the spreading of liquid metals on C is strongly dependent on chemical interaction. For the Ti-C system, $W_A^B \approx 10^3$ mJ/m^2 [42].
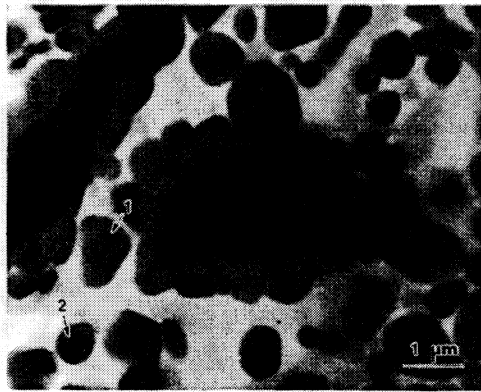
Fig. 10. Formation of TiC_x particles and separation of a TiC_x particle from the edge of a C particle.

The smaller Ti particles are consumed first through their interaction with Ni, while the larger particles are progressively consumed as one moves across the interface region, initially by the interaction with Ni and then by melting.

After the Ti particles have been completely consumed, the resulting Ti-Ni melt is initially inhomogeneous as shown in Fig. 9(a) and (b). This is a natural consequence of the fact that the powder mixture is heterogeneous and that there is a finite time required for intermixing between components once the melt has formed. The large darker regions (1) in Fig. 9(a) are voids which formed due to the melting of the Ti particles followed by capillary flow [47,48]. Within the solidified Ti-Ni melt, light and dark regions are evident. The light regions (2) are Ni rich while the dark regions (3) are Ni poor. The dark lenticular features (4) within the solidified Ti-Ni melt are C particles. Figure 9(b) shows that the C particles are covered with a TiC_x layer. The homogeneous distribution of the C particles within the solidified Ti-Ni melt as shown in Fig. 9(a) indicates that the Ti-Ni melt at least partially wets the TiC_x layer formed on the C particles. Solid-liquid systems in which the contact angle is less than 90° (i.e., partial wetting conditions) are characterized by an equilibrium spacing of solid particles in the liquid, which depends upon the contact angle, particle size, and volume of liquid [49].

As the temperature increases, the thickness of the TiC_x layer also increases. Eventually, for sufficiently large C particles, the TiC_x layer breaks up and "ejects" TiC_x particles into the Ti-Ni melt. The apparent diameter of these particles appears to be between 0.2 and 1 μm, and is independent of the reactant particle sizes. Examination reveals that the formation of these particles occurs first at the edges of the C particles. Figure 10 shows TiC_x particle which has separated from the TiC_x layer (shown by arrow 1). The break-up of the TiC_x layer enhances the reaction rate. Residual C within some of the TiC_x particles can be seen in Fig. 10 as indicated by arrow 2.

Mo does not strongly affect many of the processes observed in the partially-reacted region for several reasons: (1) the volume content of Mo is low; (2) the Mo particles form agglomerates; (3) Mo does not melt; and (4) Mo is a weak carbide former. Figure 11(a) shows a large Mo agglomerate (arrow) within the partially reacted region. As can be seen, TiC_x particles have already formed. Figure 11(b) is a close-up of a Mo particle which exhibits a diffusion layer (indicated by arrow). Elemental identification of this layer was not possible due to its small size. Because of its high melting point (~ 2600°C), Mo does not melt during the reaction. As seen in Fig. 11(b), Mo enters into solution with the Ti-Ni-C melt through the formation of an intermediate reaction layer at its surface. This process
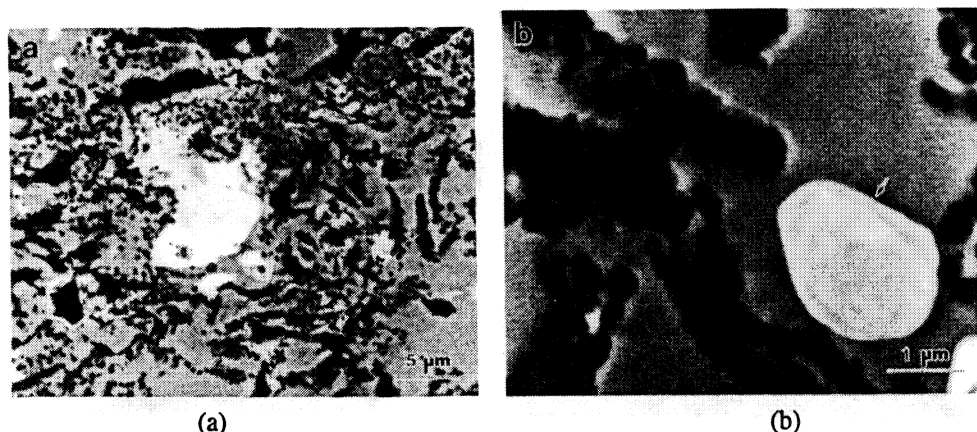
(a)   (b)

Fig. 11. (a) Large Mo agglomerate within partially reacted region; and (b) Mo particle exhibiting diffusion layer.

is apparently slower than the initial interaction between Ti and C.

Once in solution, Mo preferentially diffuses into the TiC_x phase. Figure 12(a) shows evidence of Mo within the TiC_x precipitates on a C particle (arrows). Figure 12(b) shows the carbide precipitates immediately following completion of the reaction between Ti and C. Note that the carbide precipitates exhibit a Mo-rich shell. The "rosary-bead" carbide precipitate chains break up into individual carbide particles.

3.3.3. Fully Reacted Region

After the C particles have been completely consumed, the TiC_x particles undergo a process of rapid growth by dissolution-reprecipitation and grain coalescence. The driving force for these processes is the minimization of the overall interfacial energy per unit volume (inversely proportional to the particle diameter). This process is shown in Fig. 13(a) and (b). The apparent diameter of the carbide particles in Fig. 13(a) is approximately 1 μm, while those in Fig. 13(b) is 2 μm. This indicates that the maximum temperature and cooling-rate are extremely important parameters in controlling the final particle sizes for these materials. Note the presence of the core/shell structure within the carbide particles. The concentration of Mo is higher in the shell region of the carbide particles.

4. SUMMARY AND CONCLUSIONS

For the compositions studied in this investigation, Mo was found to have a beneficial effect on the mechanical properties of TiC-Ni-based cermets produced by SHS/impact forging. The carbide particle size or particle size distribution were not strongly affected. The mean carbide particle size varied between 3.5 and 4.5 μm, while their morphology was generally spheroidal with slight faceting. The carbide particle size distributions are characteristic of a coarsened microstructure. Qualitatively, the carbide phase contiguity decreased with increasing Mo content. The 0 Mo material was observed to contain a number of flaws: voids (regions devoid of the Ni-alloy binder), interphase debonding, and

(a)   (b)
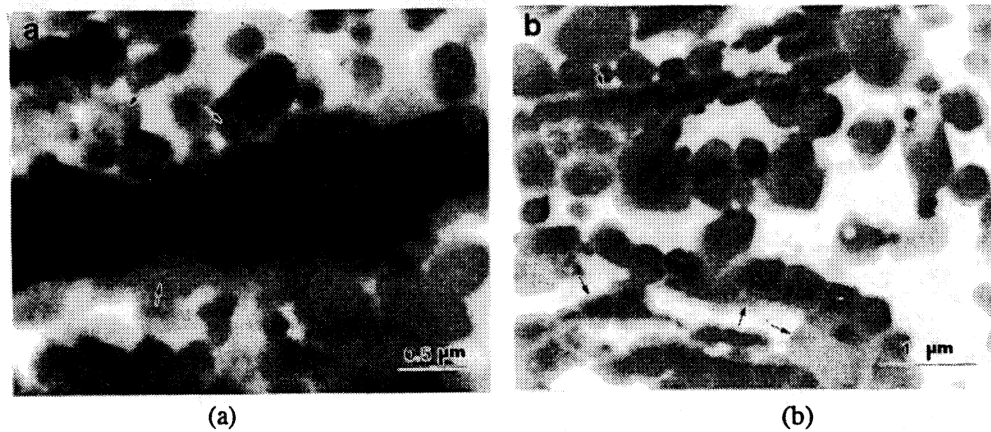
Fig. 12. (a) Evidence of Mo within the TiC_x precipitates on a C particle (arrows); and (b) "Rosary-bead" carbide precipitate chain. Note that the outer region of the carbide precipitates are Mo-rich.

binder microcracks. The voids and interphase debonding are attributed to the incomplete wetting behavior of the Ni-alloy binder melt on the carbide phase. The interphase debonding and binder microcracks are evidence of the existence of large residual elastic tensile strains at the interphase boundary and within the binder itself. These flaws drastically decreased with increasing Mo content, being nonexistent within the 8 Mo material. As in conventionally produced materials, Mo was found preferentially within the carbide phase. Mo-rich regions due to incomplete dissolution of large Mo agglomerates were observed.

The Vickers microhardness seemed to be independent of the Mo content, being approximately 13 GPa. Compressive strength, bend strength, fracture toughness, Young's moduli, and shear moduli

(a)   (b)
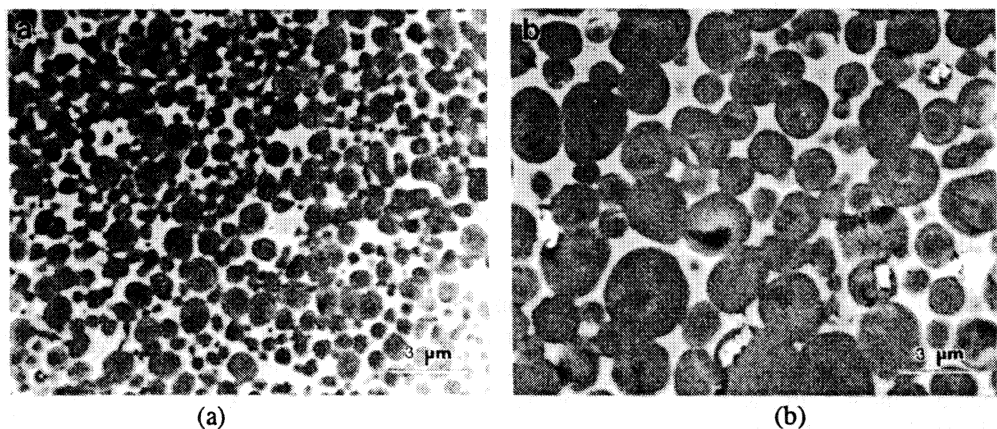
Fig. 13. Coarsening of TiC_x particles in the fully reacted region with apparent diameters: (a) 1 μm; and (b) 2 μm.

improved with increasing Mo content. The improvements are mainly attributed to the decreasing flaw density with increasing Mo content. The mean values for the 8 Mo material are 3377 MPa, 1326 MPa, 22 MPa $\cdot$ m$^{1/2}$, 340 GPa, and 131 GPa, respectively. These are comparable to conventionally produced materials. The fracture surface morphology was transgranular, indicating a strong interphase bond.

The results of the reaction arresting technique revealed the physical processes which occur within the three distinct regions of the combustion wave. The dependence of the final microstructure upon the reactant particle sizes is not strong, depending more strongly on the temperature-time history of the process.

The unreacted region is characterized by both the break-down of a scale on the Ti particles and the Ti $\alpha \rightarrow \beta$ solid-solid phase transformation. Reaction between components is limited to their contact regions.

The partially reacted region is characterized by Ti-Ni melt formation and homogenization, capillary spreading, TiC_x formation, and TiC_x particle formation. The apparent sizes of the TiC_x particles appears to be independent of either the Ti or C reactant particle sizes.

The fully reacted region is characterized by TiC_x particle coarsening and subsequent Ni melt crystallization. This indicates that the maximum temperature and cooling rate are extremely important parameters which can be controlled in order to optimize the final microstructure.

Mo does not affect the main interaction between Ti and C because the process by which it enters into solution with the Ti-Ni melt is apparently slower than the characteristic reaction time between Ti and C. It is this reaction which affects the combustion wave velocity because of its dominant exothermic nature. Once in the melt, Mo segregates itself to the TiC_x phase, resulting in the formation of the core/shell structure observed in conventionally processed materials.

ACKNOWLEDGEMENTS

REFERENCES

[1] J. F. Crider, *Ceram. Eng. Sci. Proc.*, vol. 3, 1982, p. 519.

[2] W. L. Frankhouser, K. W. Brendley, M. C. Kleszek, and S. T. Sullivan, *Gasless Combustion Synthesis of Refractory Compounds*, Noyes Publications, New Jersey, 1985.

[3] Z. A. Munir and U. Anselmi-Tamburini, *Mater. Sci. Rep.*, vol. 3, 1989, p. 277.

[4] H. C. Yi and J. J. Moore, *J. Mater. Sci.*, vol. 25, 1990, p. 1159.

[5] A. G. Merzhanov, in: *Combustion and Plasma Synthesis of High-Temperature Materials*, Z. A. Munir and J. B. Holt (Editors), VCH Publishers, New York, 1990, p. 1.

[6] A. S. Rogachev, A. S. Mukas'yan, and A. G. Merzhanov, *Dokl. Akad. Nauk SSSR*, 1987, vol. 297, pp. 1240-1243.

[7] A. S. Rogachev, V. M. Shkiro, I. D. Chausskaya, and M. V. Shvetsov, *Comb. Expl. Shock Waves*, 1988, vol. 24, pp. 720-726.

[8] A. G. Merzhanov and A. S. Rogachev, *Pure & Appl. Chem.*, 1992, vol. 64, pp. 941-953.

[9] V. L. Kvanin, V. A. Gorovoi, N. T. Balikhina, I. P. Borovinskaya, and A. G. Merzhanov, *Int. J. SHS*, vol. 2, no. 1, 1993, p. 56.

[10] Z. Y. Fu, W. M. Wang, H. Wang, R. Z. Yuan, and Z. A. Munir, *Int. J. SHS*, vol. 2, 3, 1993, p. 307.

[11] V. V. Podlesov, A. V. Radugin, A. M. Stolin, and A. G. Merzhanov, *J. Eng. Physics Thermophysics*, vol. 63, no. 5, 1993, p. 1065.

[12] E. E. Osipov, E. A. Levashov, V. N. Chernyshov, A. G. Merzhanov, and I. P. Borovinskaya, *Int. J. SHS*, vol. 1, no. 2, 1992, p. 314.

[13] G. A. Adadurov, I. P. Borovinskaya, Yu. A. Gordopolov, and A. G. Merzhanov, *J. Eng. Physics Thermophysics*, vol. 63, no. 5, 1993, p. 1166.

[14] Y. Miyamoto, M. Koizumi, and O. Yamada, *J. Am. Ceram. Soc.*, vol. 67, no. 11, 1984, p. C224.

[15] H. Klemm, K. Tanihata, and Y. Miyamoto, *J. Mat. Sci.*, vol. 28, 1993, p. 1557.

[16] J. C. Murray and R. M. German, *Met. Mat. Trans. A*, vol. 23A, 1992, p. 2357.

[17] S. D. Dunmead, J. B. Holt, and D. D. Kingman, in: *Combustion and Plasma Synthesis of High-Temperature Materials*, Z. A. Munir and J. B. Holt (Editors), VCH Publishers, New York, 1990, p. 186.

[18] S. D. Dunmead, Z. A. Munir, J. B. Holt, and D. D. Kingman, *J. Mater. Sci.*, vol. 26, 1991, p. 2410.

[19] R. V. Raman, S. V. Rele, and M. J. Paskowitz, *J. Met.*, vol. 45, no. 1, 1993, p. 54.

[20] J. C. LaSalvia, L. W. Meyer, and M. A. Meyers, *J. Am. Ceram. Soc.*, vol. 75, no. 3, 1992, p. 592.

[21] J. C. LaSalvia, M. A. Meyers, and D. K. Kim, *J. Mater. Syn. Proc.*, vol. 1, no. 2, 1994, p. 255.

[22] D. K. Kim, J. C. LaSalvia, D. A. Hoke, and M. A. Meyers, *J. Am. Ceram. Soc.*, 1995, accepted.

[23] J. C. LaSalvia, D. K. Kim, and M. A. Meyers, *J. Mat. Sci. Eng.*, 1995, submitted.

[24] A. Niiler, L. J. Kecskes, T. Kottke, P. H. Netherwood, Jr., and R. F. Benck, *Ballistics Research Laboratory Report*, BRL-TR-2951, December 1988, Aberdeen Proving Ground, MD.

[25] B. H. Rabin, G. E. Korth, and R. L. Williamson, *J. Am. Ceram. Soc.*, vol. 73, no. 7, 1990, p. 2156.

[26] H. A. Grebe, A. Advani, N. N. Thadhani, and T. Kottke, *Met. Mat. Trans. A*, vol. 23A, 1992, p. 2365.

[27] M. Humenik, Jr. and N. M. Parikh, *J. Am. Ceram. Soc.*, vol. 39, no. 2, 1956, p. 60.

[28] N. M. Parikh and M. Humenik, Jr., *J. Am. Ceram. Soc.*, vol. 40, no. 9, 1957, p. 315.

[29] *Cermets*, J. R. Tinklepaugh and W. B. Crandall (Editors), Reinhold Publishing Corporation, New York, 1960.

[30] D. Moskowitz and M. Humenik, Jr., in: *Modern Developments in Powder Metallurgy*, H. H. Hausner (Editor), Plenum, vol. 3, 1966, p. 83.

[31] G. V. Samsonov, G. T. Dzodziev, L. I. Klyachko, and V. K. Vitryanyuk, *Sov. Powder Metall. Met. Ceram.*, vol. 12, no. 4, 1972, p. 300.

[32] G. T. Dzodziev, A. A. Kal'kov, A. A. Dubrovskii, V. A. Gotlib, E. F. Korzukhina, and T. A. Shapoval, *Sov. Powder Metall. Met. Ceram.*, vol. 144, no. 4, 1983, p. 318.

[33] J. L. Ellis and C. G. Goetzel, in: *Metals Handbook: Properties and Selection: Nonferrous Alloys and Special-Purpose Materials*, 10th Edition, vol. 2, ASM International, 1990, p. 978.

[34] J. Blitz, *Fundamentals of Ultrasonics*, Butterworths, London, 1967.

[35] J. C. LaSalvia, D. K. Kim, R. A. Lipsett, and M. A. Meyers, *Met. Mat. Trans. A*, 1994, accepted.

[36] H. W. Newkirk, Jr. and H. H. Sisler, *J. Am. Ceram. Soc.*, vol. 41, no. 3, 1958, p. 93.

[37] *Metals Handbook: Properties and Selection: Stainless Steels, Tool Materials, and Special Purpose Metals*, 9th Edition, vol. 3, ASM International, 1978, p. 448.

[38] C. G. Goetzel, in: *Metals Handbook: Powder Metallurgy*, 9th Edition, vol. 7, ASM International, 1978, p. 798.

[39] G. T. Fisher II, L. L. Oden, and G. Asai, *Bureau of Mines Report of Investigations*, RI 9115, US Dept. of the Interior, 1987.

[40] M. Loshak, N. Konovalenko, T. Shapoval, and M. Dudkin, in: *Mechanical Behavior of Materials. IV. Proceedings of the Fourth International Conference*, J. Carlsson and N. G. Ohlson, Oxford (Editors), UK: Pergamon, vol. 2, 1984, p. 865.

[41] A. S. Mukasyan and I. P. Borovinskaya, *Int. J. SHS*, 1992, vol. 1, pp. 55-63.

[42] A. G. Merzhanov, A. S. Rogachev, A. S. Mukas'yan, and B. M. Khusid, *Comb. Expl. Shock Waves*, 1990, vol. 26, pp. 92-102.

[43] *Micron Metals, Inc.*, Salt Lake City, Utah.

[44] L. J. Kecskes and A. Niiler, *J. Am. Ceram. Soc.*, 1989, vol. 72, pp. 655-661.

[45] A. K. Filonenko and V. I. Vershinnikov, *Sov. J. Chem. Phys.*, 1985, vol. 3, pp. 675-682.

[46] *Cermets*, J. R. Tinklepaugh and W. B. Crandall (Editors), Reinhold, New York, NY, 1960.

[47] V. M. Shkiro and I. P. Borovinskaya, *Comb. Expl. Shock Waves*, 1976, vol. 12, pp. 828-831.

[48] A. I. Kirdyashkin, Yu. M. Maksimov, and A. G. Merzhanov, *Comb. Expl. Shock Waves*, 1981, vol. 17, pp. 591-595.

[49] R. M. German: *Liquid Phase Sintering*, Plenum, New York, NY, 1985.